Physics of Plasmas ARTICLE scitation.org/journal/php

Temporal single-surface multipactor dynamics under obliquely incident linearly polarized electric field

Cite as: Phys. Plasmas **26**, 123509 (2019); doi: 10.1063/1.5126438
Submitted: 2 September 2019 · Accepted: 5 November 2019 ·
Published Online: 3 December 2019

De-Qi Wen,[1,2,a)] Peng Zhang,[1] Yangyang Fu,[1,2] Janez Krek,[1] and John P. Verboncoeur[1,2]

AFFILIATIONS

[1]Department of Electrical and Computer Engineering, Michigan State University, East Lansing, Michigan 48824, USA
[2]Department of Computational Mathematics, Science and Engineering, Michigan State University, East Lansing, Michigan 48824, USA

[a)]wendeqi@msu.edu

ABSTRACT

It is well-known that single-surface multipactor discharges can negatively affect electromagnetic wave transmission, especially in high power microwave devices and space-based communication systems. In this work, the temporal single-surface multipactor dynamics under an obliquely incident linearly polarized electric field are investigated by particle-in-cell simulations. The results reveal that multipactor discharges highly decay by adjusting the angle, θ, between the rf electric field and the dielectric window. For plane waves with $\theta = 0$, the number of electrons as a function of time oscillates at twice the rf frequency. However, alternative oscillations decrease in magnitude at $\theta = 0.05\pi$ and disappear at $\theta = 0.15\pi$. This is because the perpendicular component of the rf electric field alternatively reinforces or reduces the restoring field and increases or decreases the secondary electron emission in half of the rf period. In addition, the electrons are forced into a few branches in the phase space of velocity and position, i.e., the electrons have a few groups of velocities at a fixed position due to the largely increased electron flight time. Finally, multipactor suppression is investigated by a simple kinetic model, by which the susceptibility diagram is obtained. This diagram shows the upper and lower boundaries gradually approach each other upon increasing θ from 0 to 0.2π, indicating reduced parameter space, in which multipactor discharge can develop.

I. INTRODUCTION

Multipactor discharge is a ubiquitous phenomenon observed in a multitude of high field radio frequency (rf) devices, such as high power microwave (HPM) sources, high voltage insulators from DC to microwaves, rf accelerators, and space-based communication systems.[1–8] Generally, it occurs when an ac electric field propagates within a metallic gap or passes a dielectric surface, which is known as two-surface or single-surface multipactor, respectively. Specifically, the latter may result in rf window breakdown with reflected power or catastrophic dielectric failure and has been a limiting factor in many wave transmission systems. Therefore, single-surface multipactor has attracted substantial research efforts.[9–17]

Analytical theory, supported by Monte Carlo simulation, on a single-surface multipactor discharge was first performed by Kishek *et al.*,[2] and susceptibility diagrams, applicable to a wide range of materials, were established in terms of the applied rf and surface dc electric fields. The susceptibility diagrams allow estimation of rf power over which the multipactor would occur. A statistical theory and deduced susceptibility curves were revisited later by Sazontov *et al.*[18] The effect of space charge on the spatial distribution of the potential, i.e., the electric field normal to the surface, was explored by Valfells *et al.*[17] This normal electric field determines the multipactor saturation state.[9] Self-consistently taking into account the space charge effect and reducing the statistic errors in Monte Carlo simulation, a full particle-in-cell (PIC) simulation tracking a large number of superparticles was primarily developed by Kim and Verboncoeur.[13] The simulations found the electron number oscillates at twice the driving frequency in the saturation state, and the corresponding trajectory of the rf field and surface normal field traces a Lissajous curve.[13] The normal field returns the electrons to strike the surface with additional energy (absorbed from the rf field). In this process, about 1% of the wave power is deposited on the dielectric surface in this parameter regime.[9] The resulting heated dielectric surface may desorb gases, potentially inducing ionization breakdown via energetic multipacting electrons.[14]

This transition of window breakdown from a vacuum multipactor discharge to an rf plasma was examined by Kim and Verboncoeur[14] by assuming various background gas pressures. Aldan also developed a model incorporating surface heating, desorption, and ionization in a dc gap.[19] The scaling law for the discharge formation time vs pressures was constructed by Lau *et al.*[20] To increase the breakdown threshold for a rf window, periodic rectangular and triangular surface structures were theoretically and experimentally proposed and shown to suppress multipactor.[21–25] In this situation, there is an oblique angle between the rf electric field and the local window surface. Additionally, in practical rf power transmission devices, it is common to have a structure where a good conductor is connected to a dielectric by an angle other than $\pi/2$, such as a flared high power microwave horn.[26] As a result, oblique incidence of an electromagnetic wave on a dielectric window is an important issue. Valfells *et al.*[12] first studied the effect of an oblique rf electric field on the susceptibility diagram of multipactor discharge by Monte Carlo simulations. The simulations were run for the given restoring dc field, which is not self-consistently calculated vs time. The temporal evolution of multipactor dynamics, such as spatio-temporal electron density, and electron dynamics in the phase space of velocity and position were missing, and the space charge effect was also physically excluded.

In this work, performing a PIC simulation[13] with space charge effect and residual net positive charge-induced normal restoring field self-consistently considered, we comprehensively investigate the multipactor dynamics under an oblique linearly polarized ac electric field and especially examine the temporal physics including multipactor absorbed power density and electron dynamics vs time and space, as well as in the phase space of velocity and position in detail. In the current simulation, we consider a system of single-surface multipactor at the vacuum side. The reduced multipactor observed in simulations is further explored by a dynamic model to examine the multipactor boundaries.

In Sec. II, the multipactor discharge configuration and the plane wave propagation direction are described, and the model assumptions are presented. For all the simulations, both the frequency and amplitude of the ac electric field are constant, implying the electromagnetic wave power is fixed. The properties of the dielectric material are determined by defining its secondary electron yield curve by Vaughan's model.[27] In Sec. III, the time-averaged surface charge density and the temporal and spatial distribution of the electron density profile are studied. The dynamics of electrons in the phase space of velocity and position are investigated for different oblique angles θ. The differences between perpendicular and oblique incidence are compared. In addition, a susceptibility diagram, consisting of two multipactor boundaries, is semianalytically obtained by deriving the electron motivation trajectory and estimating the time-averaged electron impact energy in Sec. IV. Conclusions and further discussions are presented in Sec. V, and the details of the normalized and numerical solution procedure are given in the Appendix.

II. PIC SIMULATION OF MULTIPACTOR DISCHARGE

We consider a multipactor discharge near a dielectric window, and the corresponding schematic is shown in Fig. 1. In this part, we adopt a PIC simulation[13,28] to trace the motion of electrons in the x direction and the velocities in x, y, and z directions. The Poynting vector of the electromagnetic waves is obliquely incident upon the

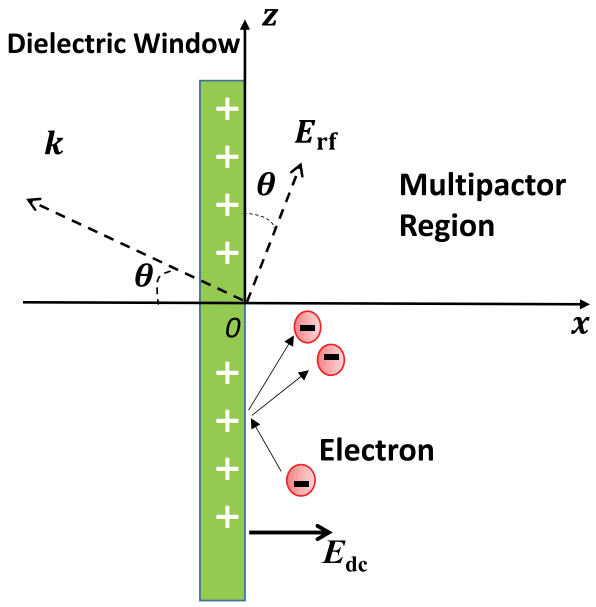

FIG. 1. Schematic (not to scale) of a multipactor discharge and plane wave propagation. The electric field oscillates and propagates in the x-z plane.

dielectric window, with angle θ, which is equivalent to the angle between the rf electric field and the window surface. The electric field in the x-z plane is considered, and the magnetic field oscillating in the y direction is neglected because the Lorentz force is generally much smaller than the electric force when the velocity of electrons is much smaller than the speed of light. The electric field components in the x, y, and z directions are given by

$$\begin{aligned} E_x &= E_{\mathrm{dc}} + E_{\mathrm{rf}} \sin\theta \sin(\omega t + \varphi), \\ E_y &= 0, \\ E_z &= E_{\mathrm{rf}} \cos\theta \sin(\omega t + \varphi), \end{aligned} \tag{1}$$

where E_{dc} is the restoring normal electric field induced by the positive charge left on the dielectric surface by secondary electron emission, $E_{\mathrm{rf}} = 3 \times 10^6$ V/m is the fixed amplitude of the rf electric field, θ is the oblique angle as stated above, $\omega = 2\pi f$, with the carrier frequency $f = 2.85$ GHz, and φ is the random initial phase.

The wavelength of electromagnetic waves in vacuum is about 0.1 m, much larger than the typical multipactor discharge length, which is a few micrometers at saturation. Thus, the external electric field is assumed to be constant in space. To self-consistently consider the space charge effect, the Poisson equation is solved with the right boundary assumed to be at infinity and grounded, i.e., the equipotential boundary, $V(x = \mathrm{Xlength}) = 0$, where Xlength is the computational domain length. In addition, we assume the right boundary has a zero value of secondary electron yield. The left boundary of the Poisson equation (right-hand side of the dielectric window in Fig. 1) has a normal electric field $E_{x,\mathrm{wall}} = \sigma_{\mathrm{wall}}/\epsilon_0$, with ϵ_0 being the vacuum dielectric constant and σ_{wall} the positive surface charge density on the dielectric wall. The total system is charge neutral, and so the positive charge density is equal to the electron space charge density $\sigma_{\mathrm{wall}} = -N_e\sigma_e$; here, N_e is the total number of superparticles and

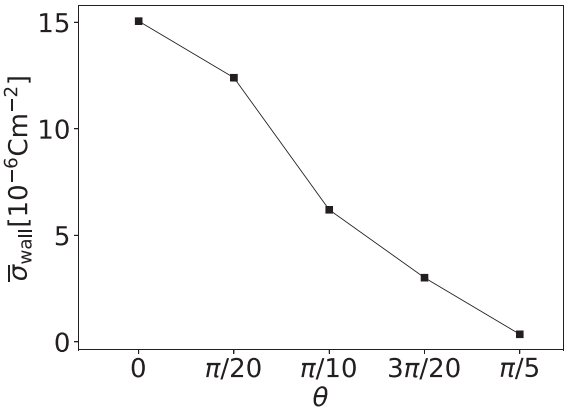

FIG. 2. The positive surface charge density vs various angles of obliqueness. The rf electric field amplitude and carrier frequency are fixed at 3 MV/m and 2.85 GHz, respectively.

$\sigma_e = N_{super}e/A_w$, with N_{super} being the weight of superparticle (the number of real particles represented by a superparticle) and A_w the dielectric window area. In all the runs, N_{super} is fixed at 5×10^9. The Poisson equation is solved on discrete uniform grids, and the resulting electric field is linearly weighted to two neighboring grids.[29] Thus, the grid cells should be small enough to resolve the space charge field, which is superimposed on the external rf electric field to push the electrons. The time step in our simulation is fixed at 3×10^{-14} s. To supply seed electrons in the beginning of all the simulations, an initially injected electron current density from the dielectric exists for the entire initial RF period, as Kim and Verboncoeur did in Ref. 13. Phases will be self-consistently diminished or increased based on the physics in part due to the phase of initial emission. Thus, the effect of the rf field phase is physically considered in the PIC simulation. The secondary electron emission for PIC simulation has been described in Refs. 27, 30, and 31 and is summarized in Sec. IV A.

III. TIME-DEPENDENT MULTIPACTOR DYNAMICS FROM PIC SIMULATIONS

As stated in Sec. II, the positive charge density σ_{wall} on the dielectric window will increase until the normal restoring field is strong enough to reduce the electron trajectories, and then the system gradually reaches a saturation state. The positive surface charge density is equal to the electron density integrated over the whole region; hence, σ_{wall} reveals the strength of the multipactor discharge. The time-averaged surface charge densities, $\overline{\sigma}_{wall}$, at the saturation state for various oblique angles are shown in Fig. 2. $\overline{\sigma}_{wall}$ almost linearly decreases and approaches zero upon increasing the oblique angle θ from 0 to 0.2π, i.e., the overall multipactor discharge gets much weaker.

To further understand the time-dependent dynamics, we show the temporal total electron number in Fig. 3. In the base case $\theta = 0$, the oscillation frequency of the electron number is twice the fundamental frequency as shown in Fig. 3(a).[13] The secondary electron yield

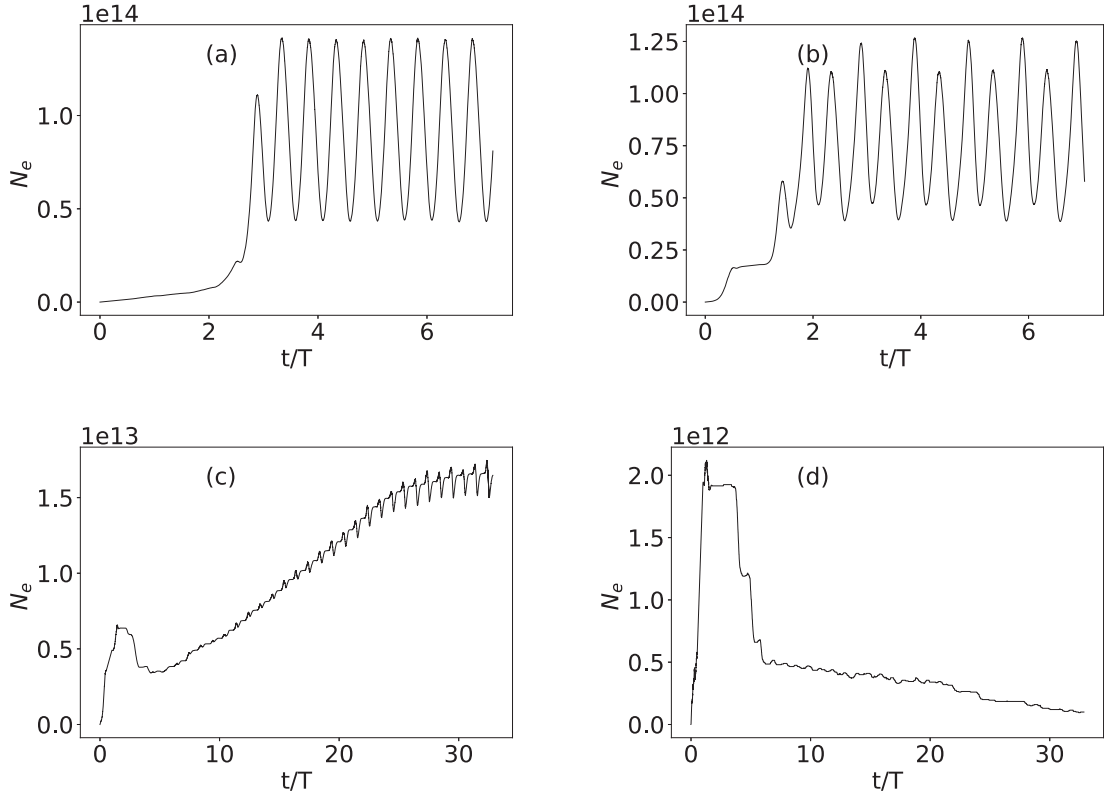

FIG. 3. The total electron number at different oblique angles: (a) $\theta = 0$; (b) $\theta = 0.05\pi$; (c) $\theta = 0.15\pi$; (d) $\theta = 0.2\pi$.

is a function of primary electron energy and angle of impact, and it is dominated by the electron impact energy.[27,32] In general single-surface multipactor, the primary electron flight time, t_0, is much smaller than the rf period, T, most electrons only see the instantaneous or a small part of the rf field phase, and thus, the electron impact energy would depend only on the field phase, at which the secondary electrons were emitted. As a result, the total number of electrons largely depends on the instantaneous rf field amplitude instead of the sign of the electric field. Ultimately, the total electron number oscillates twice within one rf period, and the two oscillations have the same amplitudes. The maximum value is about three times the minimum value as shown in Fig. 3(a). This case at $\theta = 0$ agrees well with the observations in Kim's work.[13] However, the overall amplitude of these two oscillations decreases upon increasing θ from 0 to 0.15π. The corresponding ratio of the maximum value to the minimum value at $\theta = 0.15\pi$ is around 1.1, implying that the oscillation decays with increasing θ. In addition, oscillations decay alternately faster and slower, as shown in Figs. 3(b) and 3(c), because of the smaller amplitude of the parallel component of the rf field, $E_{\mathrm{rf}} \cos\theta$, at larger θ. On the other hand, the vertical rf field component would either reinforce or reduce the restoring field, depending on the rf phase. The averaged effect over particles largely weakens one of the two oscillations. At $\theta = 0.15\pi$, even though the total number of electrons slightly decays at the beginning of the simulation, a very small part of the electrons fly out of the simulation domain before the restoring field gets strong enough to change the sign of their velocities. However, multipactor is still sustained for a longer time and finally reaches a relatively weak saturation state. At the saturation state, all the electrons would periodically return to the surface, which will be shown later. For $\theta = 0.2\pi$ in Fig. 3(d), the multipacting cannot be continuously sustained, and so the stable saturation state does not appear.

The secondary electron emission yield from the surface, δ, for the impacts averaged over one rf period is shown in Fig. 4(a) as a function of time. The corresponding normal component of the rf electric field, E_{x-rf}, is plotted in Fig. 4(b). Here, we define $\delta = S(t)/\overline{M}$, with $S(t)$ being the number of generated secondary electrons at time t and $\overline{M}$ the time-averaged impacts for one rf period. Therefore, the value of δ vs time reveals the temporal strength of the generated secondary electrons from the surface. The time-averaged value of δ is unity at saturation. We can see that δ also has two identical values within one period for $\theta = 0$, the same as the behavior of the total electron number in Fig. 3(a). With increasing θ, the second peak of δ gradually decays first and then almost approaches zero, implying no impacts between electrons and surface happen when t/T is close to an integer. This is because that the normal component of the rf electric field is negative and strong enough to deaccelerate the electrons to fly away from the surface at larger θ. The first peak of δ is enhanced at $\theta = 0.15\pi$, due to the positive normal component of the rf electric field. Even though the first peak value of δ is larger at $\delta = 0.15\pi$ than that of $\theta = 0$, the absolute number of emitted secondary electrons is indeed much smaller because of smaller impact number $\overline{M}$ at $\theta = 0.15\pi$. Thus, the disappeared alternative oscillations in Figs. 3(c)–3(d) can be clearly understood.

Figures 5(a)–5(d) show the spatiotemporal electron density distribution for various oblique angles. We can see that the maximum density appears close to the window surface and sharply decays to a small value. The peaks of the densities at the saturation state decrease from $4.5 \times 10^{19}\ \mathrm{m}^{-3}$ ($\theta = 0$) to $1.1 \times 10^{18}\ \mathrm{m}^{-3}$ ($\theta = 0.15\pi$). For the case $\theta = 0.2\pi$, we can see density peaks at the beginning stage that are induced by the background electron current and highly decrease in time. The typical length of the multipactor in the x direction is around 15 μm at $\theta = 0.15\pi$, which is significantly larger than 10 μm at $\theta = 0$. For the cases shown here, the corresponding collisionless skin depth $\delta = c/\omega_p$ for the maximum electron density is in the range of 1.6 cm–3.2 cm, which is much larger than the typical multipactor length, 15 μm. This also justifies the assumption of a spatially uniform plane wave.

The electron current density, **J**, and electric field, **E**, have three components in x, y, and z directions with zero value in the y direction, resulting in deposited power density $J_x \times E_x$ and $J_z \times E_z$, respectively. Figures 6(a)–6(d) show the total spatially averaged power density, $\mathbf{P}_t$, and its components P_x, P_y, and P_z in x, y, and z directions. We can see at $\theta = 0$ in Fig. 6(a) that the deposited power also oscillates twice within one rf period, consistent with the behavior of the temporal electron number as shown in Fig. 3(a). The deposited power has a large positive peak value and a small negative valley value. The positive part means that the electrons are accelerated and obtain energy from the electric field. On the contrary, the electrons slow down and lose energy when the power is negative. The negative value is the consequence of a small phase difference between **E** and **J**, which physically arises due to

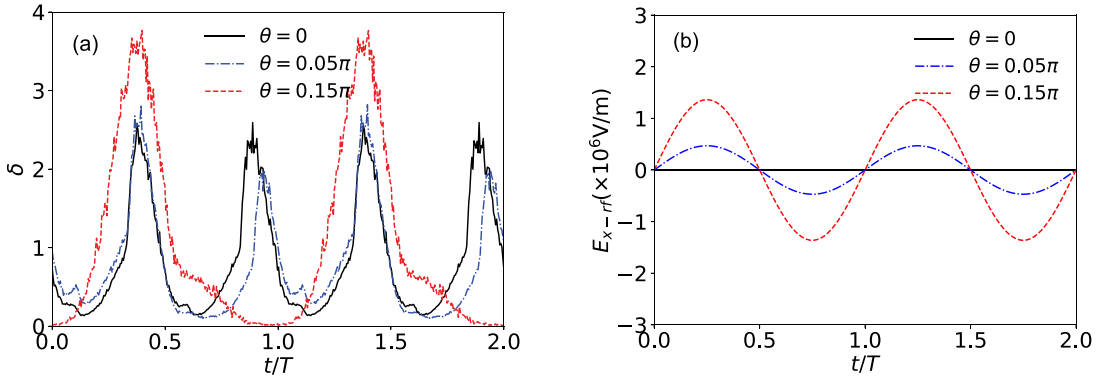

FIG. 4. (a) Secondary electron emission yield, δ, for impacts averaged over one rf period at the saturation state, varies as a function of time; (b) the normal component of the rf electric field, E_{x-rf} corresponding to (a). The oblique angle θ equals 0, 0.05π, and 0.15π.

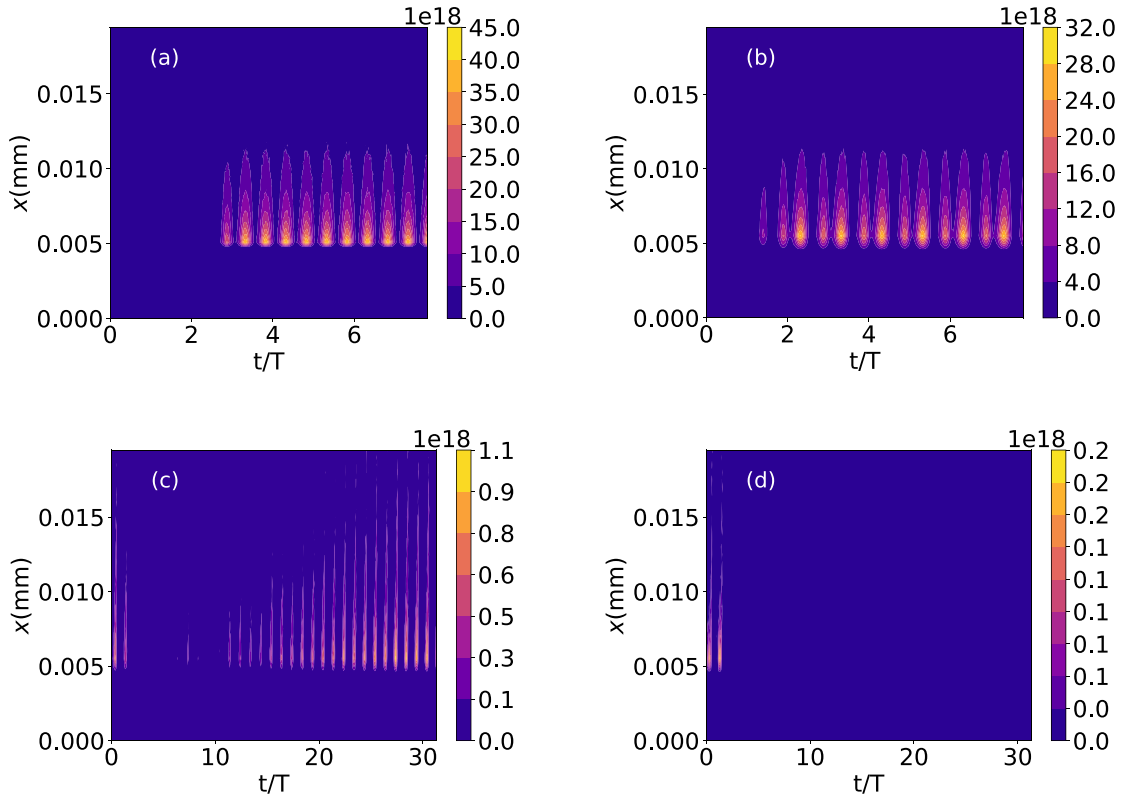

FIG. 5. The spatiotemporal electron density distribution: (a) $\theta = 0$; (b) $\theta = 0.05\pi$; (c) $\theta = 0.15\pi$; (d) $\theta = 0.2\pi$. Note that the dielectric surface is at $x = 0.0045$ mm.

electron inertia and normal component of the rf electric field. The time-averaged deposited power gives the total net power deposition and power flux to the window surface, inducing secondary electrons, whose initial energy is very low and on the order of the surface material work function, about 2 eV. With the increasing oblique angle, the ratio of the negative power and positive power gradually increases until they are equal to each other and highly reduce at $\theta = 0.2\pi$. In addition, the total power deposition is dominated by the power from the z direction field for small θ. The power deposition in the x direction has a tiny increment and also contributes to the net power absorption at $\theta = 0.15\pi$ as shown in Fig. 6(c).

Figures 7(a)–7(p) show the electron dynamics in the phase space of velocity and position, i.e., $v_x - x$, respectively. The electron velocity is reduced by the space charge electric field since it is emitted from the surface. Thus, the electrons fly through a short length in the x direction and v_x is small at $\theta = 0$, as shown in Figs. 7(a)–7(d). With the increasing oblique angle, the velocity of the electrons emitted within the range of phase $0 - \pi$ will be sharply reduced by the positive rf field $E_x \sin\theta \sin(\omega t + \varphi)$ and then change sign to strike the surface. If the velocity of one electron changes the sign again before it strikes the surface, then this electron will fly farther from the surface in the x-direction than the $\theta = 0$ case, as shown in Figs. 7(e)–7(h) and 7(i)–7(l). In addition, we find that the electrons are forced into a few branches, i.e., the electrons have a few groups of velocities at the same position, which is totally different from the case $\theta = 0$. This is because of the presence of the perpendicular components of the rf electric field, which makes the maximum electron flight time a few times longer than the rf period, within which some electrons are reaccelerated away before reaching the surface, whereas other groups of electrons would strike the surface and produce a few groups of new secondary electrons. Thus, these bundles of electrons synchronously and repeatedly remain together in time. Comparing the last three rows, we can also see that the larger electric field amplitude in the x direction, $E_{rf} \sin\theta$, induces a larger electron flight length. At $\theta = 0.2\pi$, the multipaction is not sustained and does not have a restoring field strong enough to return the electrons. Finally, the saturation state is absent as shown in Fig. 3(d).

IV. SUSCEPTIBILITY BOUNDARY

A. Model description

In this part, different from Monte Carlo simulations in Ref. 12, we develop a new kinetic model to explain the phenomenon of multipactor suppression by revisiting the multipactor susceptibility boundaries. The model developed in this work not only verifies observations of Monte Carlo simulation in Ref. 12 but also reveals the physical mechanism of the varying multipactor boundaries.

A secondary electron emitted from the dielectric has emission energy E_0 and angle ϕ, whose distribution function has the following form[30] in PIC simulation:

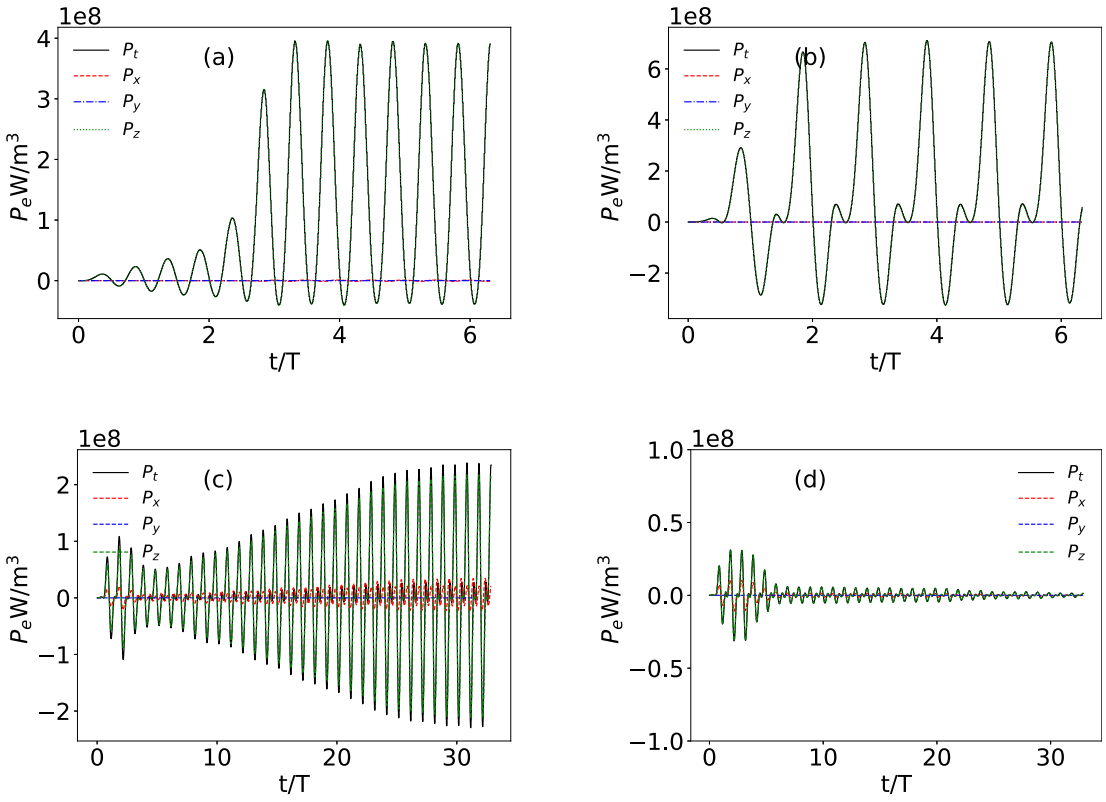

FIG. 6. The spatially averaged electron deposition power density vs time: (a) $\theta = 0$; (b) $\theta = 0.05\pi$; (c) $\theta = 0.15\pi$; (d) $\theta = 0.2\pi$. Here, T is the rf period.

$$f(E_0) = \frac{E_0}{E_{0m}^2} e^{-E_0/E_{0m}}, \tag{2}$$

$$g(\phi) = \frac{1}{2}\sin(\phi), \tag{3}$$

where E_{0m} is on the order of the work function of the dielectric window materials, which is about unity electron volt. In this work, we assume E_{0m} to be 1 eV. The mean emission energy is $E_0 = 2$ eV.

For simplicity, we have the following assumptions in the model:

(a) The secondary electron is emitted with an initial velocity only in the x direction, and other components are zero;
(b) after the flight, the electrons striking the dielectric surface are in the direction parallel to the rf electric field;
(c) the initial phase that an emitted secondary electron faces is random and uniformly distributed.[30]

The electron trajectory and velocity are analytically traced at the given rf and normal restoring electric field. The total electric field acting on electrons is given in (1). When an electron is launched with an initial velocity,

$$\begin{aligned} v_x &= v_0, \\ v_y &= 0, \\ v_z &= 0, \end{aligned} \tag{4}$$

with the mean velocity $v_0 = \sqrt{2E_0/m}$, integrating the electric field (1), and then the electron velocity could be obtained[12] at time t,

$$\begin{aligned} v_x(t) &= v_0 - \frac{eE_{dc}}{m}t + \frac{eE_{rf}}{m\omega}\sin\theta[\cos(\omega t + \varphi) - \cos(\varphi)], \\ v_y(t) &= 0, \\ v_z(t) &= \frac{eE_{rf}}{m\omega}\cos\theta[\cos(\omega t + \varphi) - \cos(\varphi)]. \end{aligned} \tag{5}$$

When an electron returns to strike the dielectric surface, the flight time t_0 should satisfy $\int_0^{t_0} v_x(t)dt = 0$; substituting into (5), we obtain

$$\left(v_0 - \frac{eE_{rf}}{m}\sin\varphi\right)t_0 - \frac{eE_{dc}}{2m}t_0^2 + \frac{eE_{rf}}{m\omega^2} \times \sin\theta[\sin(\omega t_0 + \varphi) - \sin(\varphi)] = 0. \tag{6}$$

After t_0 is solved, we can obtain the electron velocity and the corresponding impact energy when it strikes the surface. Setting the time-averaged impact energy equal to the two crossover points of the secondary electron yield (SEY) curve, which separately yield unit SEY, we can obtain the relationship between E_{dc} and E_{rf} to obtain the multipactor susceptibility boundaries. The solution procedure is described in the Appendix. Uniform initial phase distribution of φ is assumed, following previous theory-related studies.[2] One might expect that the additional rf electric field in the x direction would make the electron motion coupled to the initial phase φ. However, PIC simulation results shown in Figs. 3(a)–3(c) reveal reduced oscillation amplitude of the total electron number, whose maximum and minimum values get close to the time-averaged value, implying the absolute change in secondary electron

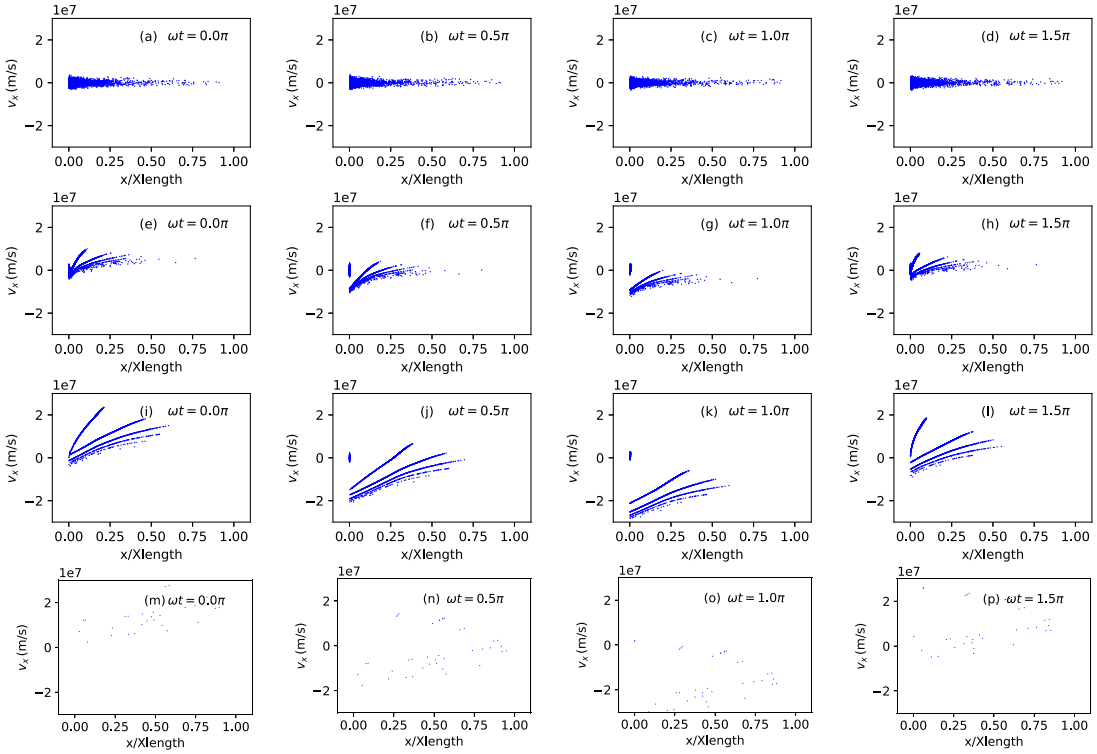

FIG. 7. The superparticle distribution in the phase space of velocity and position for four different phases: (a)–(d) $\theta = 0$; (e)–(h) $\theta = 0.05\pi$; (i)–(l) $\theta = 0.15\pi$; (m)–(p) $\theta = 0.2\pi$. Note that here the integer rf periods of phase $2n\pi$ are neglected, and the initial phase shift is set to zero in (1).

emission vs time is smaller at larger θ. Figure 4(a) shows that the reduced second peak of the relative secondary electron emission yield is compensated by the first enhanced peak value. Thus, the assumption (c) is also relatively reasonable. Additionally, we compare the model results with the simple Monte Carlo simulation in Ref. 12, which agree well in trend at $\theta = 0$, $0.056\pi(10^\circ)$, $0.12\pi(20^\circ)$, $0.42\pi(75^\circ)$. This again justifies the application of assumption (c) to a certain degree.

B. Susceptibility boundaries

In this section, the susceptibility diagrams from the kinetic model are shown in Figs. 8(a)–8(d). The horizontal axis is the normalized time-averaged dc electric field. Note that this dc field is only induced by the positive charge on the dielectric surface and the time-averaged rf component is zero. The vertical axis represents the total normalized amplitude of the rf electric field. The results in Fig. 8(a) for $\theta = 0$ are a typical case, and the physics has been revealed in the previous work; here, our motivation is to show the key features and compare them with the cases where the oblique angles are not zero. The lower and upper boundaries respond to the two crossover points (E_1 and E_2 stated in Subsection IV A), respectively, i.e., the points on the two lines make the time-averaged impact energy equal to E_1 and E_2. The rf field magnitude changes the electron impact energy for a given flight time, and the dc field affects the electron flight time, in turn to affect the electron impact energy. When the rf field is too strong or too weak, the resulting impact energy will be either lower than E_1 or higher than E_2 at a given dc electric field, yielding a SEY less than 1. Generally, increasing the dc field will shorten the flight time, and thus, a larger rf field is needed to keep the impact energy fixed at E_1 and E_2. This is the origin of the linear relationship between E_{rf} and E_{dc} for theoretical susceptibility boundaries.

The lines in Fig. 8 indicate the upper and lower boundaries at $\theta = 0, 0.05\pi, 0.15\pi$, and 0.2π. It shows the lower boundary has a decreased slope compared to the base case $\theta = 0$. This is because the existence of the perpendicular rf field increases the electron fight time on average, which has to be compensated by a larger dc restoring field to limit the flight time and to maintain the averaged impact energy equal to E_1. Although the tangential field has a smaller amplitude $E_{rf}\cos\theta$ at larger θ, the electron also gains energy from the perpendicular field $E_{rf}\sin\theta\sin(\omega t + \varphi)$, which guarantees the electron to have almost the same averaged impact energy as $\theta = 0$. For the upper boundary within the range of low E_{dc} values, we also observe a peculiar relationship between E_{dc} and E_{rf} at $\theta = 0.05\pi$ [see Fig. 8(b)], similar to Valfells *et al.* observed by single-particle Monte Carlo simulations.[12] This is attributed to the fact that the electrons are reaccelerated away from the dielectric surface before they return to strike the surface, mathematically corresponding to multiple roots for E_{dc} at fixed E_{rf}, which can satisfy the energy balance equation [see (A4) in the Appendix]. The bump gradually decays and vanishes when θ increases to 0.15π and 0.2π. From the calculations using (A3) we found that the electrons can obtain higher averaged energy from the mixed perpendicular and parallel rf field at larger θ for a given E_{dc}. On the other

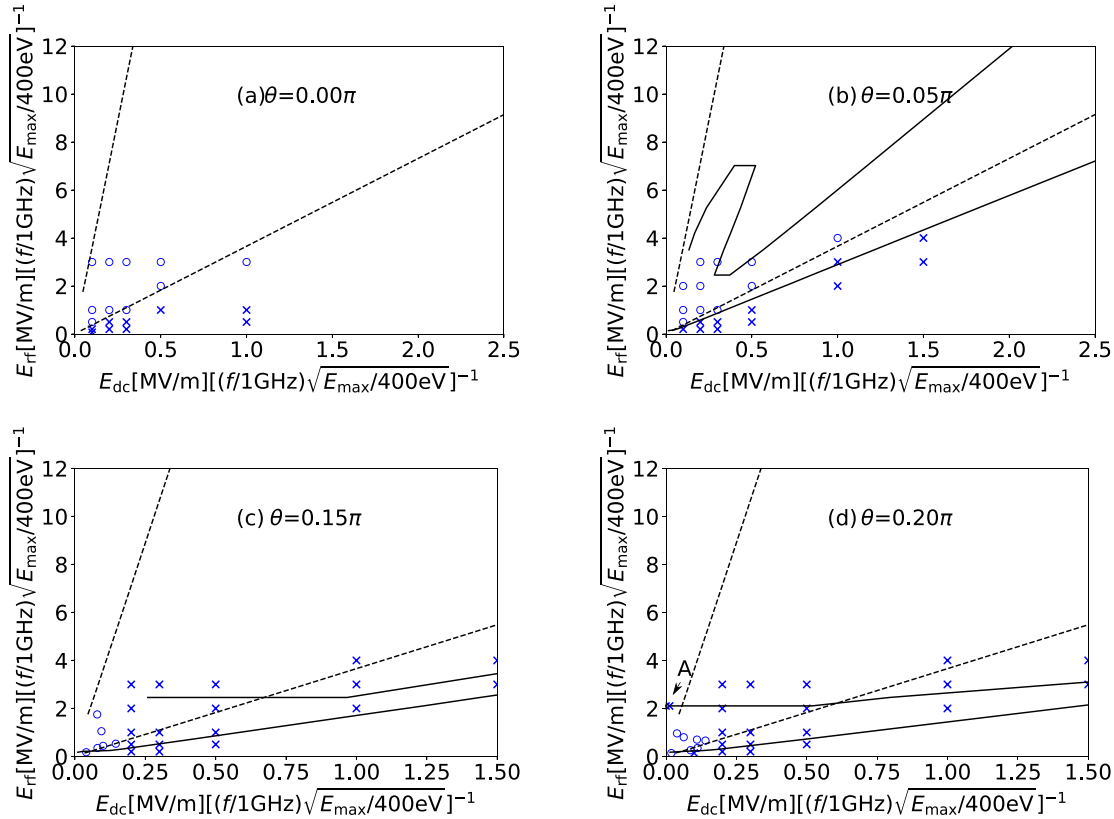

FIG. 8. Susceptibility boundaries in the space of (E_{dc}, E_{rf}) for $\delta_{max0} = 2.0$, $E_{max0} = 400$ eV, and varying oblique angles. (a) $\theta = 0$ (dashed line); (b) $\theta = 0$ (dashed line), $\theta = 0.05\pi$ (solid line); (c) $\theta = 0$ (dashed line), $\theta = 0.15\pi$ (solid line); (d) $\theta = 0$ (dashed line), $\theta = 0.2\pi$ (solid line). In (a) and (b), the blue "○" and "×" represent the point (E_{dc}, E_{rf}), where the multipactor process is observed and not observed, respectively, by PIC simulation at fixed E_{dc} and E_{rf} over the whole simulation domain in (a) and (b). In (c) and (d), the blue symbols of "○" are from full PIC simulations and represent values of time-averaged E_{dc} and fixed amplitude E_{rf}. Point A in (d) is for the case of $E_{rf} = 6$ MV/m also from the full PIC simulation, where both temporal and time-averaged values of E_{dc} are small.

hand, the larger θ in our model indicates a larger impact angle for electrons striking the dielectric surface, which gives a smaller E_2 as shown in Table I. This causes the upper boundary to move down and approach the lower boundary, resulting in a reduced multipactor susceptibility region and implying the multipactor would be harder to develop, which is in qualitative agreement with PIC simulation in Sec. III.

As a comparison, we also run simplified PIC simulations at fixed (E_{dc}, E_{rf}), i.e., the space charge effect induced spatial variation of the field is not considered, and all the particles are pushed at fixed E_{dc} and E_{rf}. The blue "o" represents the observation of multipactor at the point of (E_{dc}, E_{rf}), and the blue "×" means no multipactor. We can see that multipactors are observed within (or near) the upper and lower boundaries as shown in Fig. 8(a) ($\theta = 0$) and Fig. 8(b) ($\theta = 0.05\pi$). In Figs. 8(c) and 8(d), the multipactor is not obviously observed at most of the values of given E_{dc} from the simplified PIC simulations. For the electron emitted in the first half cycle of the rf electric field, the vertical component of the rf field enhances the given restoring dc field, thus shortening the hop time of the emitted electrons. Therefore, the electron impact energy is obviously reduced in the first half cycle, and the multipactor is suppressed. For the electron emitted in the second rf period, the electrons are accelerated away from the surface once they are emitted, giving rise to a hop time larger than half the rf period for larger θ. As the resonant condition is not satisfied, therefore, most of the secondary electron yields are continuously smaller than one (not shown here), and finally, multipactor is not observed.

TABLE I. The values of energy, E_1 and E_2, normalized to E_{max0} at different θ values.

θ	0	0.05π	0.1π	0.15π	0.2π
E_1	0.136	0.137	0.138	0.139	0.14
E_2	12.588	11.115	9.84	8.752	7.8397

For self-consistent full PIC simulations, the restoring dc field varies in time and the electron hop time also changes in time; so some particles have secondary electron yields above unity, and a balance between electron gain and loss, i.e., a weak saturation state of multipactor discharge, is ultimately obtained. The self-consistent PIC simulation results are also given by the blue "○" symbols in Figs. 8(c) and 8(d). We can see that the kinetic model gives a narrow multipactor susceptibility zone, within which the cases of saturated weak multipactor discharges are also obtained for different E_{rf} values from full PIC simulations. In addition, the varying total number of electrons in Fig. 3 reveals a strongly

oscillated restoring field on the surface, giving rise to very different motion dynamics through the whole rf period compared to the case of a given dc field. Note the time-averaged restoring field in PIC simulations might be quantitatively different from the results for a fixed restoring field in Ref. 12. Therefore, we emphasize the importance of performing a self-consistent full PIC simulation when one estimates the absolute strength of a multipactor discharge at specific parameters. The discrepancy between the kinetic model and the simplified PIC is most probably attributed to the different treatments for the electron emission angle and energy. The fixed electron emission angle and energy in the kinetic model allow for a longer electron hop time, resulting in higher probability to obtain proper impact energy and a more grazing angle, which is different from the PIC simulation. It is not that surprising because a discrepancy between simulation and theory could also be observed even for the ideal normal incidence case.[30]

V. CONCLUSIONS AND DISCUSSION

In high power microwave systems, the energetic electrons can induce multipactor discharge near an rf window and negatively affect the electromagnetic field transmission. In this work, we investigated the effect of oblique linearly polarized rf electric field on multipactor dynamics in detail. The angle θ between the Poynting vector and the normal vector of the surface varies from 0 to 0.2π. With increasing θ, we obtain three key results from PIC simulation in the range of parameters of our interest: (i) the time-averaged surface charge density and the absorbed power by electrons largely decay; (ii) at $\theta = 0$, the total number of electrons shows two symmetric oscillations within each rf period, because the electron flight time is much smaller than the rf period, and the electrons respond to electric field amplitude rather than the sign. However, at $\theta > 0$, the electrons are alternately enhanced and reduced by the rf vertical electric field component, $E_{rf} \sin\theta \sin\omega t$, resulting in a separately decreased and increased electron flight time within the first and second half rf periods. Thus, the alternative oscillation almost vanishes. (iii) The electron flight time increases and causes the electrons to be divided into a few discrete groups in phase space in terms of velocity and position, i.e., the electrons have significantly different normal velocities at a fixed position. In addition, the phenomenon of reduced multipactor discharge for various θ values from PIC simulations is also explored by a kinetic model, in which the electron trajectory and velocity are traced for a time-averaged restoring field. Setting the time-averaged impact energy equal to the two crossover points of the SEY curve, where the SEY is unity, the susceptibility diagram shows a smaller multipactor region at larger θ, implying that the multipactor is reduced.

This work gives new insights to suppress multipactor discharge. In our recent work,[28] we reported that shaping the perpendicularly incident rf electric field into a Gaussian-type waveform can help suppress the multipactor strength by an order of magnitude. The Gaussian-type waveform near the dielectric window surface can be constructed by customizing the frequencies and phases of multiple microwave signals.[33,34] Based upon the simulations in this work, designing an oblique angle between the rf electric field and the window surface contributes to improving the window breakdown threshold in wave transmission systems. As an example, a conical rf window for the high power microwave source could be used to induce an oblique angle in the case of transverse electric fields. The direction of the symmetric axis of the conical structure is parallel to the Poynting vector of the electromagnetic wave. Thus, there will always be an angle between the linearly polarized electric field and the surface, and multipactor could be expected to be reduced. It is also worth noting that the results obtained in this work are applicable only for the linearly polarized incident wave, whose electric field component has an oblique angle with the surface. In other words, if the electric field of the incident wave is polarized along the surface, then our tilted angle results cannot be used, even though the wave is obliquely incident. The obliquely incident wave with circular polarization will be considered in the future. Multipactor under multifrequency excitations[35] with oblique incident angles will also be investigated in future work.

In addition, a relatively strong resonant multipactor might occur in the oblique incidence at higher driving frequency,[7] which is beyond the scope of the current work, and will be investigated in the near future. This work does not consider the feedback of the multipactor on the electromagnetic wave, as well as the spatial distribution of the electric field. A self-consistent two-dimensional electromagnetic PIC simulation will be conducted to address these effects. Also, the electrons have nonrelativistic energies, i.e., the electron mass is constant, which may not be applicable for very intense electric fields. Thus, a modification based on relativistic theory is needed.

ACKNOWLEDGMENTS

This work was supported by the Air Force Office of Scientific Research (AFOSR) MURI Grant No. FA9550-18-1-0062.

APPENDIX: SOLUTION PROCEDURE

We introduce a normalized time $\tau = \omega t$, and the electron velocity and electric field are normalized to $\sqrt{E_{max0}/m}$ and $\omega\sqrt{mE_{max0}}/e$, respectively. Thus, the normalized electron velocity in (5) would be

$$\begin{aligned} v_x' &= v_0' - \mathcal{E}_{\rm dc}\tau + \mathcal{E}_{\rm rf}\sin\theta[\cos(\tau+\phi) - \cos\phi], \\ v_y' &= 0, \\ v_z' &= \mathcal{E}_{\rm rf}\cos\theta[\cos(\tau+\phi) - \cos\phi], \end{aligned} \tag{A1}$$

where $\mathcal{E}_{\rm dc}$ and $\mathcal{E}_{\rm rf}$ are the normalized dc electric field and rf electric field amplitude, and the electron flight time at initial phase φ satisfies

$$\begin{aligned} (v_0' - \mathcal{E}_{\rm rf}\sin\theta\cos\varphi)\tau_0 - \frac{1}{2}\mathcal{E}_{\rm dc}\tau_0^2 \\ + \mathcal{E}_{\rm rf}\sin\theta[\sin(\tau_0+\varphi) - \sin\varphi] = 0. \end{aligned} \tag{A2}$$

From (A2), we can get the corresponding flight time of electrons, τ_i, at the specific initial phase of the electric field, φ_i. Assuming a uniform distribution for the phase φ as Kishek *et al.* did in Ref. 2, we obtained the normalized and time-averaged impact energies,

$$\bar{\varepsilon} = \frac{1}{2}\int_0^{2\pi}(v_x'^2 + v_y'^2 + v_z'^2)d\varphi. \tag{A3}$$

By setting this averaged impact energy separately equal to the two crossover points $E_{1,2}$, at which the secondary electron yields are unity, the integration from 0 to 2π at the right-hand side of (A3) is numerically solved by uniformly discretizing the integral domain into N parts. Thus, we obtained the following equation:

$$\frac{1}{N}\sum_{i=1}^{N}\left[v_x'^2(\varphi_i,\tau_i)+v_z'^2(\varphi_i,\tau_i)\right]=2E_{1,2}. \tag{A4}$$

Note that the left-hand side of (A4) is a function of the normalized restoring dc electric field, $\mathcal{E}_{dc}$. For every given rf electric field, $\mathcal{E}_{rf}$, we obtained the relationship between $\mathcal{E}_{dc}$ and $\mathcal{E}_{rf}$ by adjusting $\mathcal{E}_{dc}$ to satisfy (A4). Ultimately, we obtain the susceptibility diagram.

In addition, since the electrons obtain energy from the rf electric field and strike the dielectric surface in the direction parallel to the rf electric field, i.e., the ejected angle $\xi=\pi/2-\theta$. To calculate the secondary electron yield δ in terms of electron impact energy E_i, Vaughan's empirical formula[27] is adopted as follows:

$$\delta=\delta_{max}(we^{1-w})^k, \tag{A5}$$

where δ_{max} is the maximum yield, $w=E_i/E_{max}$, with E_{max} being the impact energy, which gives δ_{max}, and $k=0.62$ for $w<1$ and $k=0.25$ for $w>1$. Thus, two values of electron impact energy, E_1 and E_2, give a yield of unity, and the value between them gives $\delta>1$. For an impact angle $\xi=\pi/2-\theta$ with respect to the x direction (see Fig. 1), E_{max} and δ_{max} are given by

$$\begin{aligned}E_{max}&=E_{max0}\left(1+\frac{k_s\xi^2}{2\pi}\right),\\ \delta_{max}&=\delta_{max0}\left(1+\frac{k_s\xi^2}{2\pi}\right),\end{aligned} \tag{A6}$$

and the corresponding $E_{1,2}$ at different θ (or ξ) values are listed in Table I. We set $\delta_{max0}=2.0$ and $E_{max0}=400\,\text{eV}$. Note that E_1 and E_2 are normalized to E_{max0} in Table I. In addition, we confirm the solutions of (A2)–(A4) numerically converge for $N\geq 2560$.

REFERENCES

[1]J. R. M. Vaughan, IRE Trans. Electron Devices **8**, 302 (1961).
[2]R. A. Kishek, Y. Y. Lau, L. K. Ang, A. Valfells, and R. M. Gilgenbach, Phys. Plasmas **5**, 2120 (1998).
[3]R. A. Kishek and Y. Y. Lau, Phys. Rev. Lett. **75**, 1218 (1995).
[4]S. Yamaguchi, S. Michizono, and S. Anami, IEEE Trans. Nucl. Sci. **39**, 278 (1992).
[5]D. H. Preist and R. C. Talcott, IRE Trans. Electron Devices **8**, 243 (1961).
[6]N. Rozario, H. F. Lenzing, K. F. Reardon, M. S. Zarro, and C. G. Baran, IEEE Trans. Microwave Theory Tech. **42**, 558 (1994).
[7]J. Power, W. Gai, S. Gold, A. Kinkead, R. Konecny, C. Jing, W. Liu, and Z. Yusof, Phys. Rev. Lett. **92**, 164801 (2004).
[8]R. A. Kishek, Phys. Rev. Lett. **108**, 035003 (2012).
[9]L.-K. Ang, Y. Y. Lau, R. A. Kishek, and R. M. Gilgenbach, IEEE Trans. Plasma Sci. **26**, 290 (1998).
[10]R. A. Kishek and Y. Y. Lau, Phys. Plasmas **3**, 1481 (1996).
[11]R. A. Kishek, Y. Y. Lau, and D. Chernin, Phys. Plasmas **4**, 863 (1997).
[12]A. Valfells, L. K. Ang, Y. Y. Lau, and R. M. Gilgenbach, Phys. Plasmas **7**, 750 (2000).
[13]H. C. Kim and J. P. Verboncoeur, Phys. Plasmas **12**, 123504 (2005).
[14]H. C. Kim and J. P. Verboncoeur, Phys. Plasmas **13**, 123506 (2006).
[15]P. Zhang, Y. Y. Lau, M. Franzi, and R. M. Gilgenbach, Phys. Plasmas **18**, 053508 (2011).
[16]A. Iqbal, J. Verboncoeur, and P. Zhang, Phys. Plasmas **25**, 043501 (2018).
[17]A. Valfells, J. P. Verboncoeur, and Y. Y. Lau, IEEE Trans. Plasma Sci. **28**, 529 (2000).
[18]A. Sazontov, V. Semenov, M. Buyanova, N. Vdovicheva, D. Anderson, M. Lisak, J. Puech, and L. Lapierre, Phys. Plasmas **12**, 093501 (2005).
[19]M. T. P. Aldan, Ph.D. thesis, University of California, Berkely, 2015.
[20]Y. Y. Lau, J. P. Verboncoeur, and H. C. Kim, Appl. Phys. Lett. **89**, 261501 (2006).
[21]A. Neuber, G. Edmiston, J. Krile, H. Krompholz, J. Dickens, and M. Kristiansen, IEEE Trans. Magn. **43**, 496 (2007).
[22]G. Edmiston, A. Neuber, H. Krompholz, and J. Krile, J. Appl. Phys. **103**, 063303 (2008).
[23]C. Chang, H. J. Huang, G. Z. Liu, C. H. Chen, Q. Hou, J. Y. Fang, X. X. Zhu, and Y. P. Zhang, J. Appl. Phys. **105**, 123305 (2009).
[24]L. Wu and L. Ang, Phys. Plasmas **14**, 013105 (2007).
[25]C. Chang, G. Z. Liu, H. J. Huang, C. H. Chen, and J. Y. Fang, Phys. Plasmas **16**, 083501 (2009).
[26]C. Chang, G. Liu, C. Tang, C. Chen, and J. Fang, Phys. Plasmas **18**, 055702 (2011).
[27]J. R. M. Vaughan, IEEE Trans. Electron Devices **40**, 830 (1993).
[28]D. Q. Wen, A. Iqbal, P. Zhang, and J. P. Verboncoeur, Phys. Plasmas **26**, 093503 (2019).
[29]J. P. Verboncoeur, Plasma Phys. Controlled Fusion **47**, A231 (2005).
[30]R. Kishek and Y. Y. Lau, Phys. Rev. Lett. **80**, 193 (1998).
[31]V. P. Gopinath, J. P. Verboncoeur, and C. K. Birdsall, Phys. Plasmas **5**, 1535 (1998).
[32]J. R. M. Vaughan, IEEE Trans. Electron Devices **36**, 1963 (1989).
[33]M. L. D. S. S. Femandez-Gutierrez, J. Browning, and J. Watrous, J. Vac. Sci. Technol., B **33**, 031203 (2015).
[34]A. Yue, R. Harper, D. Black, D. Plumlee, T. Akinwande, W. Chern, M. Worthington, J. Cippola, and J. Browning, "An industrial magnetron using gated field emission arrays for phase–control," in International Vacuum Nanoelectronics Conference, Cincinnati, USA, 22–26 June (2019).
[35]A. Iqbal, J. Verboncoeur, and P. Zhang, Phys. Plasmas **26**, 024503 (2019).